

Phase Diagram of the Non-Reciprocal Cahn-Hilliard Model and the Effects of Symmetry

Martin Kjøllesdal Johnsrud ¹ and Ramin Golestanian ^{1,2}

¹*Max Planck Institute for Dynamics and Self-Organization (MPI-DS), D-37077 Göttingen, Germany*

²*Rudolf Peierls Centre for Theoretical Physics, University of Oxford, Oxford OX1 3PU, United Kingdom*

(Dated: 11 March 2025)

Interactions between active particles may be non-reciprocal, breaking action-reaction symmetry and leading to novel physics not seen in equilibrium systems. In this work, we study the phase diagram for the non-reciprocal Cahn-Hilliard (NRCH) model with different types of symmetry—discrete and continuous—and examine the effects of non-reciprocity on phase separation. The models are analyzed by drawing the full linear stability diagrams, indicating the onset of phase separation, allowing us to demonstrate how non-reciprocity gives rise to out-of-equilibrium steady states with non-zero currents. These observations are robust to noise and valid in a large part of parameter space. By describing the effects of symmetry on conserved, non-reciprocal models, this work adds to our understanding of the rich phase-behavior of such models.

I. INTRODUCTION

The physical properties of active matter—comprised of soft matter systems, living or artificial, which continually consume energy—have been the subject of extensive investigations in recent decades^{1–5}. Depending on the mechanisms that underlie the non-equilibrium activity, some of the very basic properties that apply to passive matter will no longer hold for active matter systems. In particular, the action-reaction symmetry exemplified by Newtons third law relies on forces derived from an underlying common interaction potential, which is something one cannot expect in effective descriptions of many active systems such as living organisms. Such *non-reciprocal* interactions have recently been a topic of interest in active matter, as it is an important feature of effective chemically-mediated^{6–10} or hydrodynamically-mediated^{11,12} interactions, the social interaction of swarms¹³, or in models of the brain^{14,15}. Moreover, it has been proposed that naturally occurring non-reciprocal interactions in chemically active systems may have played a role in the emergence of early forms of life^{16–18}. A similar action-reaction asymmetry, exhibited by condensed living matter, is *odd* elasticity or viscosity^{19–21}. Non-reciprocal interactions are also present in non-active systems driven out of equilibrium, such as driven dusty plasmas^{22–25}, magnetic systems^{26,27} or Bose-Einstein condensates²⁸. More generally, introducing non-reciprocal interactions is one of the simplest way to break equilibrium, making it useful as a theoretical tool for exploring the behavior non-equilibrium states of matter^{13,29–35}.

Non-reciprocal systems, or more generally non-equilibrium systems, may exhibit *exceptional points*^{36,37}. These were first considered as features of quantum systems, appearing in models of quantum chaos³⁸, \mathcal{PT} -symmetric systems^{39,40}, optical wave-guides⁴¹, and atomic orbitals⁴²; all systems where gain and loss result in non-Hermitian terms in the Hamiltonian. In non-

reciprocal systems, exceptional points appear in the linearized dynamics of the system, represented by the linear stability matrix^{13,43,44}. This matrix is in general non-Hermitian due to the broken action-reaction symmetry, and there may therefore be points in parameter space where it becomes defect, its eigenvalues complex, and the corresponding eigenvectors coalesce. Exceptional points in non-equilibrium physics promise to be a fruitful avenue for novel physical effects, such as the recently demonstrated critical fluctuations in driven-dissipative Bose-Einstein condensates⁴⁵ or non-equilibrium extensions of $O(N)$ models^{31,46,47}.

In equilibrium statistical physics, the Cahn-Hilliard model is a widely used phenomenological model for phase separation^{48,49}. The model describes the dynamics of conserved scalar fields $\varphi_a(\mathbf{x}, t)$ relaxing to minimize its free energy $F[\varphi]$. The Non-Reciprocal Cahn-Hilliard (NRCH) model extends this model by introducing non-reciprocal interactions that cannot be described in terms of minimizing free energy^{43,44}. This model has recently been shown to exhibit phase behavior beyond that of its well-studied reciprocal counterpart^{43,44,50–52}.

In this Article, we explore the phase diagram of two restricted versions of the NRCH, one with a $SO(2)$ continuous rotational symmetry and one with reduced discrete C_4 -symmetry (see Figure 1). These restricted models allow us to fully characterize their phase diagram at the linear level. We explore how the different characters of these symmetries—continuous and discrete—affect the phase behavior of out-of-equilibrium models. The symmetries are inherited by the linear-stability diagrams, effectively reducing the number of parameters in the continuous case. The symmetry further affects the phase separated state. While, in the discrete case, an energy barrier leads to distinct phases separated by a finite thickness domain wall, there is no barrier in the continuous case, leading to “continuous phase separation”. We further explore how these effects persists even when the system is driven out of equilibrium by non-reciprocal interactions.

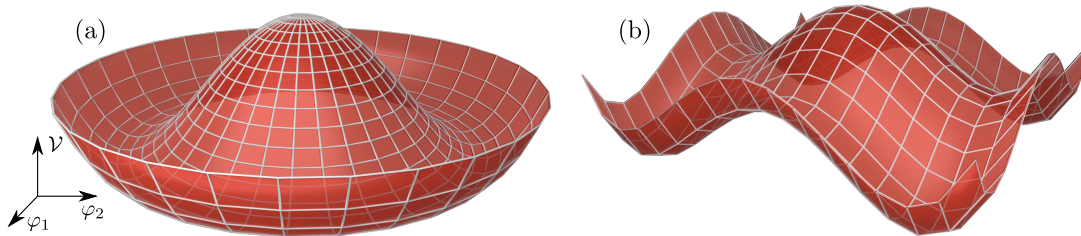


FIG. 1. (a) The Mexican hat potential of the model with continuous SO(2) symmetry. (b) The potential of the model with discrete C_4 symmetry.

II. THE MODEL

The model we consider consists of two real scalar fields, $\varphi_a(\mathbf{x}, t)$, $a \in \{1, 2\}$. These fields represent a density fluctuation at time t and position \mathbf{x} . The reciprocal interactions are due to a free energy density,

$$\mathcal{F}[\varphi] = \frac{1}{2} \nabla \varphi_a \cdot \nabla \varphi_a + \mathcal{V}(\varphi_a), \quad (1)$$

where summation is implied. The total free energy reads $F = \int d\mathbf{x} \mathcal{F}$. The two models are defined by their potential $\mathcal{V}(\varphi)$. The potential of the SO(2) model

$$\mathcal{V}_{\text{cs}}(\varphi_a) = \frac{r}{2} \varphi_a \varphi_a + \frac{u}{4} (\varphi_a \varphi_a)^2. \quad (2)$$

If $r \geq 0$, the potential has one global minimum at $\varphi_a = 0$, whereas for $r < 0$ the potential takes the characteristic Mexican hat shape illustrated in Figure 1. The potential is a function of $\varphi_a \varphi_a$ only, which is a construction that is invariant under rotations and reflections (e.g. $\varphi_1 \rightarrow -\varphi_1$) in the field space. These transformations form the Lie group O(2). The dynamics arising from this potential corresponds to Model B in the classification of Halperin and Hohenberg⁵³. The symmetry is reduced to SO(2) with the introduction of a non-reciprocal term $\alpha \epsilon_{ab} \varphi_b$ in the equations of motion (see below).

To represent an example with *discrete symmetry*, we choose the potential

$$\mathcal{V}_{\text{ds}}(\varphi_a) = \sum_a \left[\frac{r}{2} \varphi_a^2 + \frac{u}{2} \varphi_a^4 \right], \quad (3)$$

which is not invariant under continuous rotations, as illustrated in Figure 1. However, \mathcal{V}_{d} is invariant under operations in D_4 , the dihedral group of order 8 corresponding to the symmetries of a square. These operations are rotations with $n\pi/2$ radians in addition to reflections, e.g. $\varphi_1 \rightarrow -\varphi_1$. This is a discrete group, similar to the symmetry group of the single-field Cahn-Hilliard $O(1) \cong D_2$, and in the same way gives rise to a phase separation with a well-defined domain wall. The introduction of a non-reciprocal term restricts the symmetry to C_4 , namely, the cyclic group of order 4.

In an equilibrium model, the chemical potential of field φ_a is $\mu_a = \frac{\delta F}{\delta \varphi_a}$. This definition implies $M_{ab} = \frac{\delta \mu_a}{\delta \varphi_b}$ is

symmetric. This matrix represents the thermodynamic forces acting *on* field (species) a *by* field (species) b , and the symmetry of the matrix implies that the interactions are reciprocal. We now add a term $\tilde{\mu}_a$ to the chemical potential that gives rise to an anti-symmetric part of M_{ab} , thus corresponding to non-reciprocal interactions. By stipulation, such a term cannot be derived from a free energy. In both models, we introduce a minimal non-reciprocal term $\tilde{\mu}_a = \alpha \epsilon_{ab} \varphi_b$ so that $\frac{\delta \tilde{\mu}_b}{\delta \varphi_b} = \alpha \epsilon_{ab}$, where ϵ_{ab} is the anti-symmetric Levi-Civita tensor, with $\epsilon_{12} = -\epsilon_{21} = 1$. This coupling has recently been studied in^{43,44}, and more general non-reciprocal extensions have been proposed in Ref⁵⁴.

The field φ_a obeys the conservation law

$$\partial_t \varphi_a + \nabla \cdot \mathbf{j}_a = 0, \quad (4)$$

where the flux \mathbf{j}_a is given by thermodynamic forces (affinities) that arise from gradients in the chemical potential, namely, $\mathbf{j}_a = -\Gamma \nabla \mu_a$, with Γ being a mobility. The governing dynamical equations thus read

$$\partial_t \varphi_a = \Gamma \nabla^2 \left[\frac{\partial \mathcal{V}}{\partial \varphi_a} - \nabla^2 \varphi_a + \alpha \epsilon_{ab} \varphi_b \right]. \quad (5)$$

III. LINEAR STABILITY

We now construct phase diagrams for the two cases that represent different symmetries by using linear stability analysis. We study the response of the system to small perturbations around a homogeneous state, represented by $\bar{\varphi}_a$. Inserting $\varphi_a(\mathbf{x}, t) = \bar{\varphi}_a + \delta \varphi_a(\mathbf{x}, t)$ into the equations of motion, we obtain the leading order contribution in Fourier space as follows

$$\partial_t \delta \varphi_a(\mathbf{q}, t) = -q^2 \Gamma M_{ab} \delta \varphi_b(\mathbf{q}, t). \quad (6)$$

The matrix $M_{ab} = \frac{\delta \mu_a}{\delta \varphi_b} \Big|_{\bar{\varphi}}$ depends on the specific choice for the potential, and thus reflects the effects of the underlying symmetry.

A. Continuous Symmetry

We first analyze the rotationally invariant potential, choosing $\bar{\varphi}_a = (\bar{\varphi}, 0)$ without loss of generality, which

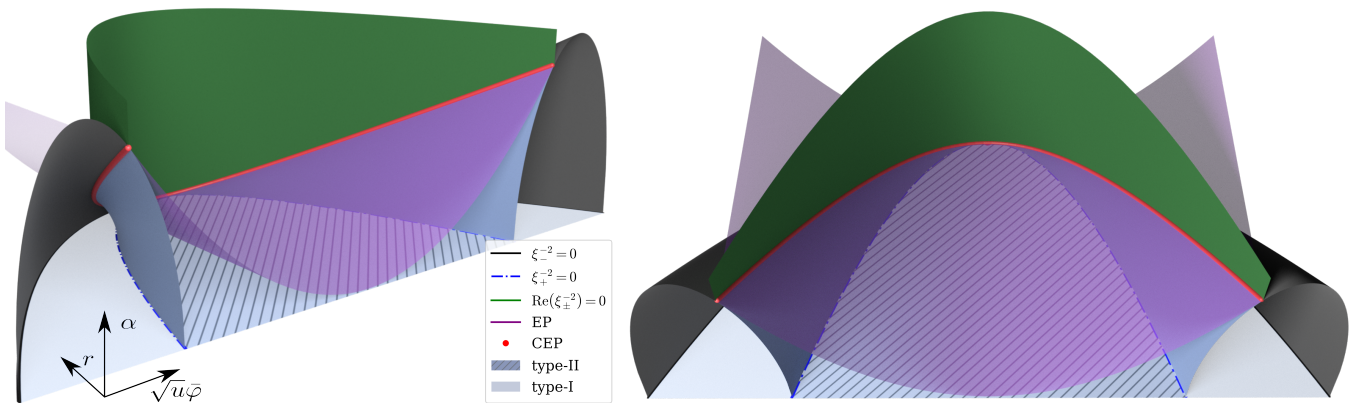


FIG. 2. The linear phase diagram of the model with continuous symmetry. The exceptional plane is highlighted in purple, and the planes between the stable, type-I unstable, and type-II unstable are highlighted in black, blue, and green, respectively. The red line is the intersection of all these surfaces.

yields

$$M_{ab} = \begin{pmatrix} q^2 + r + 3u\bar{\varphi}^2 & \alpha \\ -\alpha & q^2 + r + u\bar{\varphi}^2 \end{pmatrix}. \quad (7)$$

The corresponding eigenvalues, namely,

$$\lambda_{\pm} = q^2 + r + 2u\bar{\varphi}^2 \pm \sqrt{(u\bar{\varphi}^2)^2 - \alpha^2}, \quad (8)$$

encode the stability of the homogeneous solution. A perturbation $\delta\varphi$ will decay if the real part of the corresponding eigenvalue is positive, implying that the homogeneous state $\bar{\varphi}$ is stable. Since the q^2 term always contributes positively, the least stable eigenvalues can be obtained via $\xi_{\pm}^{-2} \equiv \lambda_{\pm}(q \rightarrow 0)$, which can be used to define correlation lengths ξ_{\pm} in terms of the three free parameters, r , $\sqrt{u\bar{\varphi}}$, and α . For $r > 0$, all values of $\bar{\varphi}$ result in stable solutions. Therefore, to look for instabilities, we set $r \leq 0$. The critical region defined by $\text{Re}(\xi_{\pm}^{-2}) = 0$, therefore, forms a two-dimensional surface in the three-dimensional parameter space. This is illustrated by the surfaces in Figure 2. Additional angles are shown in the Supplementary Material⁵⁵.

The base of this diagram is the $\alpha = 0$ surface. We choose $\alpha > 0$, without loss of generality. At $\alpha = u\bar{\varphi}^2$, we have $\xi_{+}^{-2} = \xi_{-}^{-2}$. In reciprocal systems, this indicates a degeneracy where two independent eigenmodes have the same eigenvalue. When we deal with non-reciprocal systems, and thus non-Hermitian matrices, we are no longer guaranteed that the eigenvectors of M_{ab} span the full vector space of perturbations. At this exceptional point (EP)^{36,56}, the eigenvalues coincide because the two eigenmodes $\delta\varphi_1$ and $\delta\varphi_2$ align, rendering the matrix M_{ab} defective. As there are three free parameters and the exceptional points are given by one equation, namely, $\alpha = u\bar{\varphi}^2$, the full set of exceptional points forms a 2D surface, which we denote as the exceptional plane. This is illustrated in purple in the Figure 2. Above the exceptional plane, the two eigenvalues become complex, and the perturbations will no longer decay or diverge monotonically: they exhibit oscillatory behavior. Here, we

have $\text{Re}(\xi_{\pm}^{-2}) = r + 2u\bar{\varphi}^2$, and, therefore, both modes transition from stable to unstable at the same surface, defined via $r = -2u\bar{\varphi}^2$. The intersection between the critical and the exceptional planes can be called critical exceptional points (CEPs)⁴⁵, also corresponding to a Hopf bifurcation in the terminology of dynamical systems⁵⁷. These CEPs are parameterized as follows

$$(\sqrt{u\bar{\varphi}}, r, \alpha) = (s, -2s^2, s^2), \quad s \in \mathbb{R}, \quad (9)$$

and illustrated by the red line in Figure 2. On this line, the two eigenmodes align and are both critical.

To better present the phase diagram, we now examine various two-dimensional slices that can be obtained by fixing one of the parameters. Setting $\alpha = 0$ gives the diagram of Model B for $n = 2$ fields, with $\xi_{\pm}^{-2} = r + (2 \pm 1)u\bar{\varphi}^2$. This is illustrated in Figure 3(a), and is the base of the diagram in Figure 2. At $r = \bar{\varphi} = 0$, the correlation lengths diverge. This is a critical point corresponding to the onset of phase separation. Starting in the white region of the diagram, where $u\bar{\varphi}^2 > |r|$, we have $\xi_{\pm}^{-2} > 0$, and thus both modes are stable. Upon further lowering $\bar{\varphi}$, we reach a line in the diagram at $u\bar{\varphi}^2 = |r|$ – shown as a black line in Figure 2 – where $\xi_{-}^{-2} = 0$ and the corresponding eigenmode transitions from stable to unstable. Therefore, perturbations in this direction in φ -space ($\delta\varphi_2$ in this case) will grow exponentially.

Looking back at the Mexican hat potential illustrated in Figure 1, this corresponds to a point inside the ring of minima, and perturbations that would correspond to the Goldstone mode in a spontaneous symmetry breaking scenario (i.e. the orthogonal to the radial direction). The mode corresponding to perturbations in the radial direction ($\delta\varphi_1$ in this case) remains stable. This holds in the light blue area labeled “type-I unstable”, where there is one unstable mode. At $u\bar{\varphi}^2 = |r|/3$, illustrated by a blue dash-dotted line, the second mode also transitions from stable to unstable. The area where both modes are unstable is highlighted as dark blue and hashed, with the label “type-II unstable”.

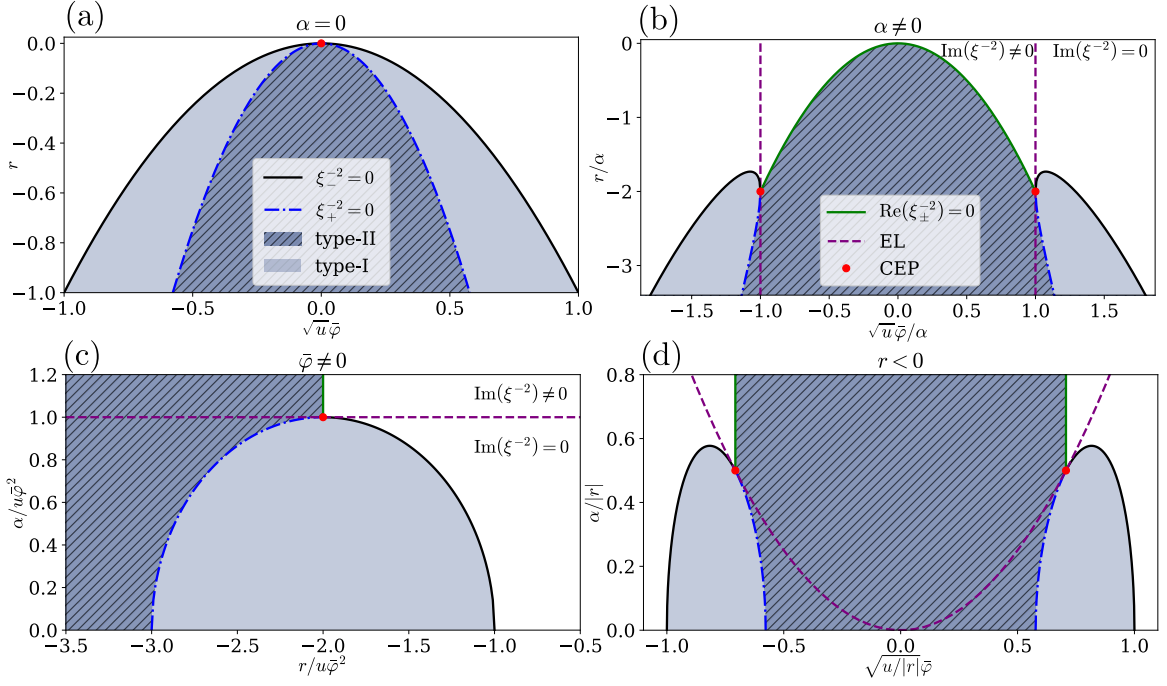


FIG. 3. The four non-trivial slices of the full three-dimensional phase diagram shown in Figure 2. Panel (a) corresponds to the equilibrium case $\alpha = 0$, while panels (b)-(d) illustrate three orthogonal slices for finite α , at constant α , $\bar{\varphi}$, and r , respectively. Light blue and hashed areas mark the type-I and type-II unstable regions. Black, blue dash-dotted, and green lines separate stable and type-I, type-I and type-II, and stable and type-II, respectively. The purple dashed line marks the exceptional points, and the red dot marks the critical exceptional points where all the lines intersect.

Assuming all parameters are non-zero, we may re-scale the correlation lengths by either of them, thus eliminating one parameter. For example, ξ_{\pm}^{-2}/α depend only on r/α and $\sqrt{u}\bar{\varphi}/\alpha$. Any two slices where $\alpha = \text{const.} \neq 0$ are thus equivalent as they are related by a scale transformation. There are therefore three additional non-trivial two-dimensional slices, illustrated by in Figure 3(b)-(d). Their intersection with the three-dimensional surface is shown in Fig. S3 in the SM⁵⁵.

We first focus on the $\alpha = \text{const.}$ slice, illustrated in Figure 3(b). The equations for the critical lines of the real eigenvalues are

$$\frac{r}{\alpha} = -2 \frac{u\bar{\varphi}^2}{\alpha} \pm \sqrt{\frac{u^2\bar{\varphi}^4}{\alpha^2} - 1}, \quad \sqrt{u}|\bar{\varphi}| > \alpha. \quad (10)$$

New to this diagram are the exceptional lines $\sqrt{u}\bar{\varphi} = \pm\alpha$, illustrated by purple dashed lines in Figure 3(b). Outside these lines, the diagram is similar to the $\alpha = 0$ diagram, while between them, the correlation lengths become complex and the region with one stable mode vanishes. The critical line is here given by

$$r = -2u\bar{\varphi}^2, \quad u|\bar{\varphi}| \leq \alpha, \quad (11)$$

and is highlighted in green, in Figure 3(b), while the intersections of this line with the critical exceptional lines are illustrated as red dots.

Next, we consider the $\sqrt{u}\bar{\varphi} = \text{const.}$ slice, illustrated in Figure 3(c). Below the exceptional line, the critical

lines form two quarter-circles, which meet at the critical exceptional point, defined by

$$\left(\frac{r}{u\bar{\varphi}^2} + 2\right)^2 + \left(\frac{\alpha}{u\bar{\varphi}^2}\right)^2 = 1, \quad (12)$$

while above the exceptional line, the critical line is given by the vertical line $r/(u\bar{\varphi}^2) = -2$.

Finally, the slice where $r = \text{const.}$ (as normalized by $|r|$) is illustrated in Figure 3(d). The equation for the critical lines below the exceptional line is

$$\frac{\alpha}{|r|} = \sqrt{-1 + 4 \frac{u\bar{\varphi}^2}{|r|} - 3 \left(\frac{u\bar{\varphi}^2}{|r|}\right)^2}, \quad (13)$$

while above it, the critical line is again given by vertical lines, defined by $\sqrt{u/|r|}\bar{\varphi} = \pm 1/\sqrt{2}$.

B. Discrete Symmetry

We now apply this analysis to the model with a square potential. The linear stability matrix is then

$$M_{ab} = \begin{pmatrix} q^2 + r + 6u\bar{\varphi}_1^2 & \alpha \\ -\alpha & q^2 + r + 6u\bar{\varphi}_2^2 \end{pmatrix}, \quad (14)$$

which has the eigenvalues

$$\lambda_{\pm} = q^2 + r + 3u(\bar{\varphi}_1^2 + \bar{\varphi}_2^2) \pm \sqrt{9u^2(\bar{\varphi}_1^2 - \bar{\varphi}_2^2)^2 - \alpha^2}. \quad (15)$$

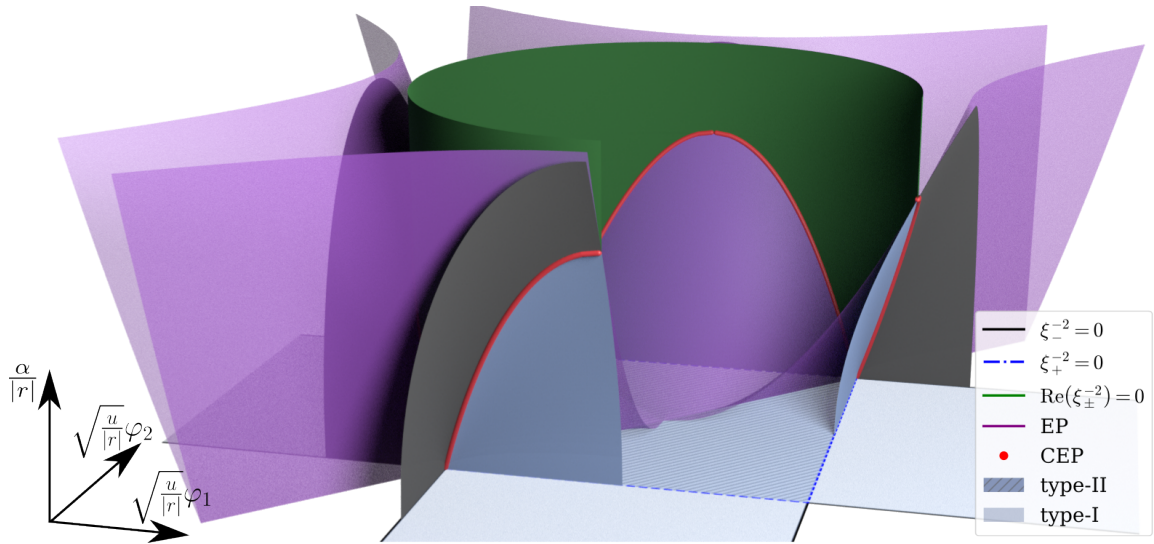


FIG. 4. The linear phase diagram of the model with discrete symmetry, scaled by $|r|$. Light blue and hashed areas mark the type-I and type-II unstable regions. Black, blue, and green planes separate stable and type-I, type-I and type-II, and stable and type-II regions, respectively. The exceptional plane is highlighted in purple, and the red line marks the critical exceptional points where all the planes intersect.

Since the eigenvalues depend on both $\bar{\varphi}_1^2$ and $\bar{\varphi}_2^2$, the full phase diagram requires another dimension to visualize. For this model, we focus on a 3D slice of the full 4D diagram as shown in Figure 4. This cross section is related to any other 3D slice via a choice of scaling, which in this case is chosen to be $|r|$. The inverse-squared correlation lengths defined via $\xi_{\pm}^{-2} = \lambda_{\pm}(q \rightarrow 0)$ as above are then given as follows

$$\xi_{\pm}^{-2} = -|r| + 3u(\bar{\varphi}_1^2 + \bar{\varphi}_2^2) \pm \sqrt{9u^2(\bar{\varphi}_1^2 - \bar{\varphi}_2^2)^2 - \alpha^2}. \quad (16)$$

Where the eigenvalues are real (i.e. outside the exceptional plane) we can find the critical surface by solving $\xi_{\pm}^{-2} = 0$, e.g. for $\bar{\varphi}_2$, which yields

$$\bar{\varphi}_2 = \sqrt{\frac{|r|^2 + \alpha^2 - 6u|r|\bar{\varphi}_1^2}{6u(|r| - 6u\bar{\varphi}_1^2)}}, \quad (17)$$

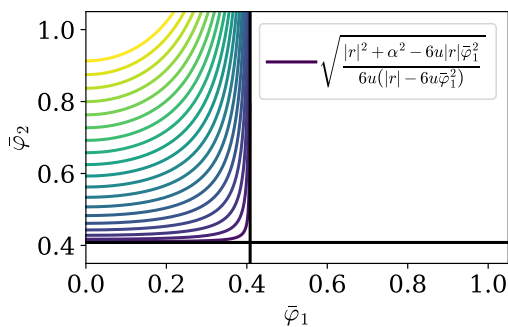


FIG. 5. The critical line for $\alpha/|r| \in [0, 2]$. Brighter colors in the plot indicate higher values of α .

with a similar solution for $\bar{\varphi}_1$. This sector, which is plotted for $u\bar{\varphi}_1^2/|r| \in [0, 1/\sqrt{6}]$ in Figure 5, represents one eighth of the total solution set, with the rest being obtained by applying the operations of D_4 . The critical surface is highlighted in green in Figure 4.

For $\alpha = 0$ the critical lines are straight, where $\sqrt{u/|r|}\bar{\varphi}_1$ or $\sqrt{u/|r|}\bar{\varphi}_2$ are $\pm \frac{1}{\sqrt{6}} \approx \pm 0.4$. As α is increased, the critical lines become curved, asymptotically approaching the $\alpha = 0$ lines for large values of the fields. The exceptional plane, shown in purple in Figure 4, is given by a set of hyperbolae defined via $u|\bar{\varphi}_1^2 - \bar{\varphi}_2^2| = \alpha/3$, where we again have chosen $\alpha > 0$ for concreteness. Inside the area bounded by the exceptional surface, i.e. the subset containing the origin, the critical surface is given by the circle $u(\bar{\varphi}_1^2 + \bar{\varphi}_2^2) = |r|/3$ where $\text{Re}(\xi_{\pm}^{-2}) = 0$, which is shown in green in Figure 4.

The intersection of the critical surface (highlighted as green in Figure 4) and the exceptional surface (highlighted as purple in Figure 4) is the critical exceptional line, which is shown in red in Figure 4 [see the corresponding equivalent plot for the continuous symmetry case, in Figure 3(d)]. These are located at the intersections of the circle of radius $1/\sqrt{3}$ and the hyperbolae with semi-major axis $\sqrt{\alpha/(3|r|)}$. For $\alpha > |r|$ there are no such points, for $\alpha = 0$ and $\alpha = |r|$ there are four, while for $\alpha/|r| \in (0, 1)$ there are eight, corresponding to the elements of D_4 . These observations can be seen in the two-dimensional slices of the phase diagram shown in Figure 6. Additional variations of such plots are presented in the SM⁵⁵.

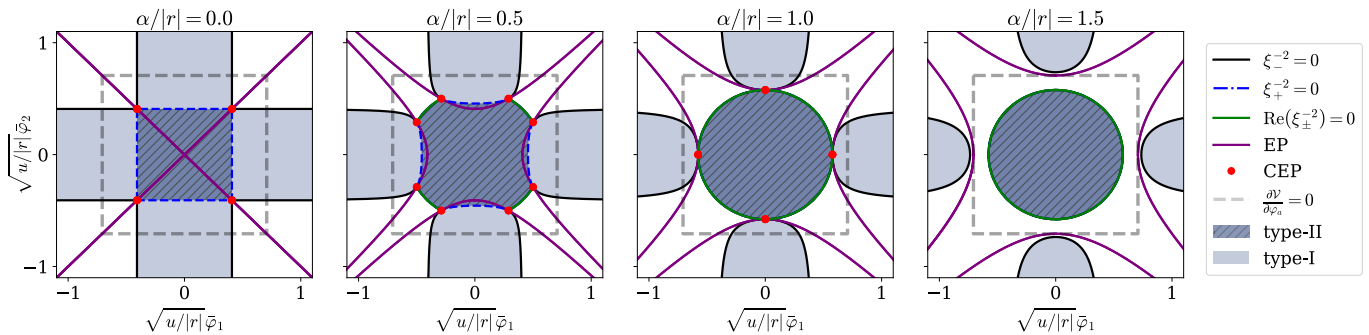


FIG. 6. Constant α slices of the phase diagram illustrated in Figure 4. The gray dashed lines represent the line connecting the minima of the potential illustrated in Figure 1(a), and form a square centered at the origin and with side lengths $\sqrt{u/|r|}\bar{\varphi} = \sqrt{2}$. Light blue and hashed areas mark the type-I and type-II unstable regions. Black, blue dash-dotted, and green lines separate stable and type-I, type-I and type-II, and stable and type-II, respectively. The purple line marks the exceptional points, and the red dot marks the critical exceptional points where all the lines intersect.

IV. PHASE SEPARATION AND NESS

When a mode is unstable, a perturbation of the homogeneous state will grow exponentially, meaning that the system cannot maintain a homogeneous state, and instead undergoes phase separation. The $\alpha = 0$ phase diagram in Figure 3 resembles the one-field ($n = 1$) double-well Cahn-Hilliard model⁴⁸. In that case, the hashed inner region is stable, and is separated by the spinodal to the metastable region $u\bar{\varphi}^2 \in (|r|, |r|/3)$ shaded blue. Here, perturbations will not grow exponentially, but a phase-separated system will have lower free energy and is thus thermodynamically favored. In the case of $n = 2$, however, this region is unstable, not metastable. The absence of a metastable homogeneous state for the SO(2)-model is a consequence of the set of minima of the potential being *connected* due to the spontaneously broken continuous symmetry of the system, in contrast to the C_4 model, which is phenomenology closer to that of the $n = 1$ Cahn-Hilliard. After adding the non-reciprocal term α , the corresponding steady-state may no longer be an equilibrium-like, current-free state, but rather a non-equilibrium steady-state (NESS). Still, we may apply similar analysis for insight into these states. We now discuss the phenomenology of phase separation, in and out of equilibrium, for the two cases.

A. Discrete Symmetry

For $\alpha = 0$, the C_4 system forms phases separated by a domain wall whose thickness is independent of the size of the system. Take the special case of $\bar{\varphi}_i = \varphi^*(0, -1)$, where $\varphi^* = \sqrt{|r|/(2u)}$ is the absolute value of the fields in the minima of the potential, i.e., the average is midway between two minima in the square potential landscape illustrated in Figure 1. Due to the decoupled nonlinearities of the square model, this system admits an exact solution, in the thermodynamic limit, similar to the well-known domain-wall solution of the one-field Cahn-

Hilliard model⁴⁸, namely

$$\varphi_1(\mathbf{x}, t) = \varphi^* \tanh[(x - x_0)/\ell], \quad (18a)$$

$$\varphi_2(\mathbf{x}, t) = -\varphi^*, \quad (18b)$$

where $\ell = \sqrt{2/|r|}$ is the domain wall thickness, which results from a trade-off between the surface tension term $\nabla^4\varphi$ and the potential term $r\nabla^2\varphi$. This domain wall profile is, in fact, valid for any average composition $\bar{\varphi}$. As discussed in the previous chapter, there may be more than two phases, but the walls between them will still have a hyperbolic tangent profile with the same length scale ℓ .

For $\alpha \neq 0$, the considerations become more complicated. As demonstrated recently, the central part of the phase diagram gives rise to traveling wave states⁴³. However, at least where α is not too large, the logic of a trade-off between potential and gradient energy—which gives rise to the finite domain wall—still applies. As illustrated in Figure 7, numerical simulations show that states with small α and $\bar{\varphi}$ still form separate phases, whose traveling domain walls are well approximated by a hyperbolic tangent with a thickness ℓ . In fact, these traveling states may be fully characterized in the thin-wall, low-activity regime, in which their velocity is proportional to the activity and inversely proportional to their size. See `video_1.mp4` in⁵⁵ for further illustration.

B. Continuous Symmetry

In the case of the Mexican hat potential illustrated in Figure 1, all points corresponding to $\bar{\varphi} = \varphi' \equiv \sqrt{|r|/u}$ define the *connected* ground state manifold. Any two points on this manifold obey a generalization of the common tangent space construction⁵⁸, and, consequently, the minimum of the free energy will therefore no longer be two homogeneous phases separated by a thin domain wall. Instead, the field can interpolate between two minimum values taking only values in or near the bottom

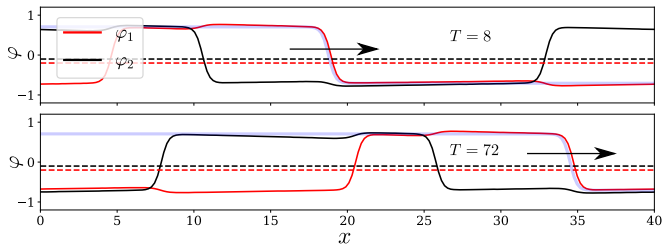


FIG. 7. The domain wall of thickness ℓ with the profile of the hyperbolic tangent, light blue, compared to numerical solutions for small α and $\bar{\varphi}$. Parameters are $u = -r = 10$, $\alpha = 2$, $(\bar{\varphi}_1, \bar{\varphi}_2) = -(0.1, 0.2)$.

of the potential. The assumption of two phases with a domain wall separating them is therefore not valid anymore; the system will consist of one continuously changing phase.

We can find an exact solution for the SO(2) model in the case of $\bar{\varphi} = 0$, corresponding to a slice of the phase diagram of the last section where the entire plane, for $r < 0$, is unstable^{51,54}. This solution has the form

$$\varphi_1(t, \mathbf{x}; \mathbf{k}) = A(k) \sin \phi(t, \mathbf{x}; \mathbf{k}), \quad (19a)$$

$$\varphi_2(t, \mathbf{x}; \mathbf{k}) = A(k) \cos \phi(t, \mathbf{x}; \mathbf{k}), \quad (19b)$$

$$\phi(t, \mathbf{x}; \mathbf{k}) = \mathbf{k} \cdot \mathbf{x} - \omega(k)t. \quad (19c)$$

Inserting this into the equation of motion Eq. (5) with the rotationally invariant potential, we obtain the following requirements for the solution to be valid

$$\omega(k) = \alpha k^2 \Gamma, \quad uA(k)^2 = -r - k^2. \quad (20)$$

Note that $\varphi_a(t, \mathbf{x}; \mathbf{k})$ solves the full non-linear equations of motion and is only possible due to the rotational symmetry of these equations. The solution is illustrated in Figure 8. The plot on the left shows the fields in real space, in the direction parallel to the wave vector \mathbf{k} . We may also visualize the configuration in (φ_1, φ_2) -space by following the line parametrized by x , shown on the right, where the minimum of the potential is indicated by dashed black lines. This can be thought of as mapping the circle $x \in S^2$ into field space, with shorter wavelength solutions corresponding to the mapping winding around the origin more times.

Linear stability analysis from substituting $\varphi_a(t, \mathbf{x}) = \varphi_a(t, \mathbf{x}; \mathbf{k}) + \delta\varphi_a(\mathbf{x})$ into Eq. (5), as detailed in Appendix A, reveals that although there may be unstable higher \mathbf{k} solutions, the longest wavelength solution is always stable. The velocity of the wave is controlled by the non-reciprocal parameter, with $\alpha = 0$ corresponding to continuous phase separation. As α increases, the wave starts to move. This traveling solution is an example of a non-equilibrium steady-state solution⁵¹.

Decreasing further below $r = 0$ yields shorter wavelength solutions. Minimizing the free energy density $\mathcal{F} = -\frac{3}{4}uA^2$ corresponds to maximizing the amplitude of the wave. The global minimum is the state with

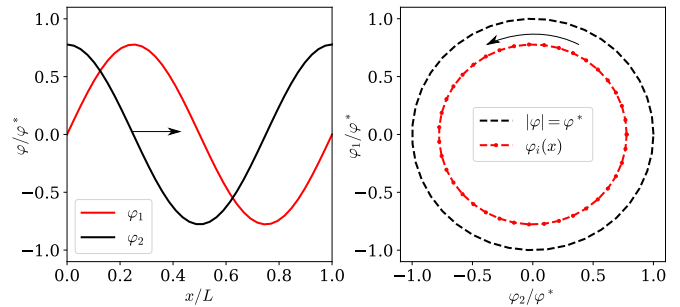


FIG. 8. The traveling wave solution for $\bar{\varphi} = 0$. To the left, the fields are plotted in one dimension of real space, parallel to the wave vector. On the right, the same configuration is shown in field space.

the longest wavelength $k = 2\pi/L$ where L is the system size, while solutions with higher wave numbers are metastable states, at least for $\alpha = 0$. Assuming $|r| \gg k^2$, the amplitude of the wave is $A \approx \sqrt{-r/u}$, corresponding to mapping the circle in field space around the bottom of the potential, as illustrated in Figure 8. In the metastable states for which $k = 2\pi n/L$ and $n > 1$ the circle is mapped n times around the brim of the hat. As n increases, the amplitude of the wave decreases as the kinetic term of the free energy acts as a tension in the line. When $|r| < k^2$, Eq. (19) no longer corresponds to a stationary solution of the equations of motion, neither stable, metastable nor unstable, as the tension has become too high. This solution is closely related to the topological defects this model admits⁵², and the general analysis holds for small finite $\bar{\varphi}$, see `video_2.mp4` in⁵⁵ for further illustration.

We may also write down an approximate solution for $\alpha = 0$ close to the minimum of the potential $\bar{\varphi} = \sqrt{-r/u}$,

$$\varphi_1(t, \mathbf{x}; \mathbf{k}) = \delta \cos 2\phi(\mathbf{x}; \mathbf{k}) - \bar{\varphi}, \quad (21a)$$

$$\varphi_2(t, \mathbf{x}; \mathbf{k}) = 2\sqrt{\bar{\varphi}\delta} \cos \phi(\mathbf{x}; \mathbf{k}), \quad (21b)$$

$$\phi = \mathbf{k} \cdot \mathbf{x}, \quad \varphi' = \sqrt{|r|/u}, \quad \delta = \varphi' - \bar{\varphi}. \quad (21c)$$

We show in Appendix B that for $\delta \ll \varphi'$ and in the long wavelength limit, this is a good approximation of the stationary solution. While the previous solution corresponds to mapping a line parallel to \mathbf{k} around the brim of the hat, this solution can be visualized as mapping this same loop to a small sector of the brim. This is illustrated in Figure 9, where the analytical solution is plotted in gray, together with the numerical solution and the deviation between them. The relaxation of the system towards this solution is illustrated in `video_3.mp4`⁵⁵.

V. CONCLUSION

In this article, we have explored the phase behavior of the non-reciprocal Cahn-Hilliard model. By choosing two

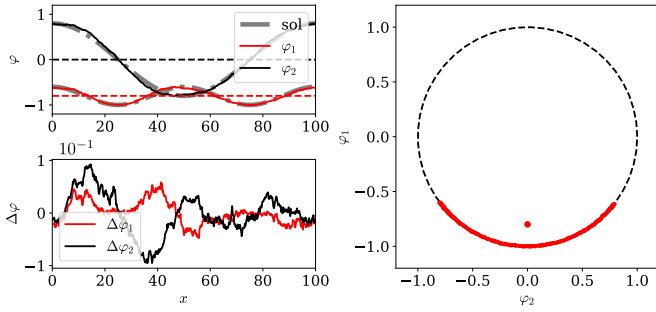


FIG. 9. The approximate solution for $\bar{\varphi} \approx \varphi'$ is shown top left in gray, while the numerical solution is overlaid in red and black. Bottom left shows the deviation between analytical and numerical solutions, including noise $D = 2 \times 10^{-4}$. The right panel shows the solution in φ_i space. Parameters are $u = -r = 40$, $(\varphi_1, \varphi_2) = -(0.8, 0)$.

reduced models—one with rotational invariance in field space and one without—we can fully characterize the linear behavior and see the effect of continuous symmetry on phase separation. The main behaviors observed are homogeneous configurations, static phase separation—continuous or with a well-defined domain wall—and non-equilibrium steady states with non-zero currents. Using this construction we have shown the effect of a continuous and connected symmetry on phase separation, where there is no well-defined domain wall. This effect remains in the case of traveling wave states where the phases chase each other due to non-reciprocal interactions.

In addition, we start to see a glimpse of the rich behavior close to the transition between static and traveling states, which linear analysis can not capture. This complicated, chaotic seeming behavior has been shown in recent simulations of both particle systems⁵⁹ and the NRCH⁵⁴. This is an area—the transition between regions dominated by the chasing behavior and the equilibrium behavior—which more sophisticated tools are needed to characterize. We believe the results from such work will uncover interesting effects that further illuminate the complex behavior of active matter. The investigation will probe the frontier between two different but simple states, the static and traveling waves, and it is exactly near such boundaries that complexity tends to arise. We will relegate such studies to future work.

ACKNOWLEDGMENTS

The Authors would like to thank Giulia Pisegna and Jacopo Romano for stimulating discussions. We acknowledge support from the Max Planck School Matter to Life and the MaxSynBio Consortium which are jointly funded by the Federal Ministry of Education and Research (BMBF) of Germany and the Max Planck Society.

Appendix A: Linear stability of $\bar{\varphi} = 0$ solution

We test the stability of the solution presented in section IV B by inserting $\varphi_a(t, \mathbf{x}) = \varphi_a(t, \mathbf{x}; \mathbf{k}) + \delta\varphi_a(\mathbf{x})$ in the equations of motion and expanding to first order in $\delta\varphi_a$. We note that, to linear order

$$(\varphi + \delta\varphi)^2(\varphi_a + \delta\varphi_a) = A^2\varphi_a + (A^2\delta_{ab} + 2\varphi_a\varphi_b)\delta\varphi_b. \quad (\text{A1})$$

Using this, we write down the linear equation of motion

$$\partial_t \delta\varphi_a = \Gamma \nabla^2 \left[(r - \nabla^2 + uA^2)\delta_{ab} + 2u\varphi_a\varphi_b + \alpha\epsilon_{ab} \right] \delta\varphi_b. \quad (\text{A2})$$

In contrast to the homogenous solution, the overall operator ∇^2 will now act on φ . We can expand the non-linear term using the chain rule. For an arbitrary function $f(x)$, if we define $A^2\mathcal{O}_{ab}f(x) \equiv \nabla^2[(A^2\delta_{ab} + 2\varphi_a\varphi_b)f(x)]$, we have

$$A^2\mathcal{O}_{ab} = 2 \left[(\nabla^2\varphi_a)\varphi_b + \varphi_a(\nabla^2\varphi_b) + 2(\nabla\varphi_a) \cdot (\nabla\varphi_b) + 2\left((\nabla\varphi_a)\varphi_b + \varphi_a(\nabla\varphi_b) \right) \cdot \nabla + \left(\frac{A^2\delta_{ab}}{2} + \varphi_a\varphi_b \right) \nabla^2 \right].$$

As $\varphi_1 \propto \sin\phi$ and $\varphi_2 \propto \cos\phi$, we have the following properties

$$\nabla\varphi_1 = \mathbf{k}\varphi_2, \quad \nabla\varphi_2 = -\mathbf{k}\varphi_1, \quad \nabla^2\varphi_a = -k^2\varphi_a. \quad (\text{A3})$$

We can therefore write $\nabla\varphi_a = \mathbf{k}\epsilon_{ab}\varphi_b$, and so in Fourier space where $\nabla \rightarrow -i\mathbf{q}$, the operator is

$$A\mathcal{O}_{ab} = -4k^2(\varphi_a\varphi_b + \epsilon_{ac}\epsilon_{bd}\varphi_c\varphi_d) - 4i\mathbf{k} \cdot \mathbf{q} (\varphi_a\epsilon_{bd}\varphi_d + \epsilon_{ac}\varphi_c\varphi_b) - q^2(A^2\delta_{ab} - 2\varphi_a\varphi_b). \quad (\text{A4})$$

We notice that \mathcal{O} is a symmetric matrix. Writing out the components explicitly, we find

$$\mathcal{O}_{11} = 4k^2 - 4i\mathbf{k} \cdot \mathbf{q} \sin 2\phi + q^2(1 + 2\cos^2\phi), \quad (\text{A5})$$

$$\mathcal{O}_{22} = 4k^2 + 4i\mathbf{k} \cdot \mathbf{q} \sin 2\phi + q^2(1 + 2\sin^2\phi), \quad (\text{A6})$$

$$\mathcal{O}_{12} = 4i\mathbf{k} \cdot \mathbf{q} \cos 2\phi + q^2 \sin 2\phi, \quad (\text{A7})$$

and $\mathcal{O}_{12} = \mathcal{O}_{21}$. The equation of motion, in Fourier space, can then be written as $\partial_t \delta\varphi_a = -\Gamma K_{ab} \delta\varphi_b$, where

$$K_{ab} = q^2[(r + q^2)\delta_{ab} + \alpha\epsilon_{ab}] + uA^2\mathcal{O}_{ab}. \quad (\text{A8})$$

The stability of the traveling wave solution is given by the signs of the real parts of the eigenvalues of K . Modes with positive eigenvalues are stable, while modes with negative are unstable. For two-by-two matrices, the eigenvalues are given by the trace and determinant. We have

$$\text{Tr } K = 2q^2(r + q^2) + x^2 \text{Tr } \mathcal{O}, \quad (\text{A9})$$

$$\det K = q^4 [(r + q^2)^2 + \alpha^2] + q^2(r + q^2)x^2 \text{Tr } \mathcal{O} + x^4 \det \mathcal{O}, \quad (\text{A10})$$

where $x^2 = uA^2$, and after some calculations, we obtain

$$\text{Tr } \mathcal{O} = 8k^2 + 4q^2 \quad (\text{A11})$$

$$\det \mathcal{O} = 16[k^4 + k^2q^2 + (\mathbf{k} \cdot \mathbf{q})^2] + 3q^4. \quad (\text{A12})$$

Thus, we can calculate the eigenvalues of K , as follows

$$\lambda_{\pm} = q^2(r + q^2) + 2(2k^2 + q^2)x^2 \pm \sqrt{q^4(x^4 - \alpha^2) - (4x^2\mathbf{k} \cdot \mathbf{q})^2}. \quad (\text{A13})$$

If we insert the amplitude criterion, $x^2 = uA^2 = |r| - k^2$ into the eigenvalue, we obtain

$$\lambda_{\pm} = q^2(|r| + q^2 - 2k^2) + 4k^2(|r| - k^2) - 2q^2k^2 \pm \sqrt{(|r| - k^2)^2[q^4 - (4\mathbf{k} \cdot \mathbf{q})^2] - \alpha^2q^4}. \quad (\text{A14})$$

The most unstable mode is the one with a negative sign when the perturbation is orthogonal to the traveling wave. Furthermore, a non-zero value for α contributes to making the solution more stable. The most unstable mode is therefore obtained by setting $\alpha^2 = \mathbf{k} \cdot \mathbf{q} = 0$,

which yields

$$\lambda_- = q^4 + 4k^2(|r| - k^2) - q^2k^2. \quad (\text{A15})$$

By assumption, $k^2 < |r|$, so only the last term can make the solution unstable. If k has the minimum value for the wavevector, $k_0 = 2\pi/L$ where L is the linear system size, then $q^2 \geq k^2$. Thus $q^4 - q^2k^2 \geq 0$ and $\lambda_- > 0$. This shows that the long wavelength solution is always stable. The marginal case, when $|r| = k^2$, corresponds to the constant solution $\varphi_a = 0$. There may exist solutions where $k = 2\pi n/L$ for $n > 1$, which corresponds to wrapping a line in the domain off $\varphi_a(\mathbf{x})$ several times around the center of the potential, but in the $\alpha = 0$ case, at least, this is a metastable state.

Appendix B: Approximate solution

We now insert the configurations Eq. (21) into the equations of motion of the field. We have

$$\varphi^2 = \delta^2 \cos^2 2\phi - 2\bar{\varphi}\delta \cos 2\phi + \bar{\varphi}^2 + 4\bar{\varphi}\delta \cos^2 \phi, \quad (\text{B1})$$

$$= \bar{\varphi}^2 - 2\bar{\varphi}\delta + \mathcal{O}(\delta^2). \quad (\text{B2})$$

The left-hand sides of the equation of motion vanish by assumption, as the configurations are time-independent, while the right-hand sides are

$$\Gamma \nabla^2 \{ [r - \nabla^2 + u(\bar{\varphi}^2 + 2\bar{\varphi}\delta)] \} (\delta \cos 2\phi - \bar{\varphi}) + \mathcal{O}(\delta^3) = -4\delta\Gamma k^2 [r + 4k^2 + u(\bar{\varphi}^2 + 2\bar{\varphi}\delta)] \cos 2\phi + \mathcal{O}(\delta^3), \quad (\text{B3})$$

$$\Gamma \nabla^2 \{ [r - \nabla^2 + u(\bar{\varphi}^2 + 2\bar{\varphi}\delta)] \} \sqrt{\bar{\varphi}\delta} \cos \phi + \mathcal{O}(\delta^{5/2}) = -2\sqrt{\bar{\varphi}\delta}\Gamma k^2 [r + 4k^2 + u(\bar{\varphi}^2 + 2\bar{\varphi}\delta)] \cos \phi + \mathcal{O}(\delta^{5/2}). \quad (\text{B4})$$

We now use $\bar{\varphi}^2 = \varphi^{*2} + \mathcal{O}(\delta) = -r/u + \mathcal{O}(\delta)$ to rewrite $r + u(\bar{\varphi}^2 + 2\bar{\varphi}\delta) = -2\bar{\varphi}\delta$. Thus, when we let $\delta, k^2 \rightarrow 0$, the right-hand side of the equations of motion vanish as $\mathcal{O}(\delta^2k^2, \delta k^4)$ and $\mathcal{O}(\delta^{3/2}k^2, \delta^{1/2}k^4)$, which are faster than the amplitudes of the solutions, ensuring convergence.

Appendix C: Numerical methods

The simulations are performed using finite difference methods in one dimension, giving a discretized set of coupled stochastic ODEs,

$$\partial_t \varphi_{a,n} = \nabla_{nm}^2 \Gamma \mu_{a,m} + \sqrt{\frac{2D}{\Delta x}} \nabla_{nm} \xi_{a,m}, \quad (\text{C1})$$

on which apply the Euler-Maruyama method for time-stepping. To guarantee detailed balance in the equilibrium ($\alpha = 0$) case, also in the space-discretized equations, it is important that the discretized Laplacian is

exactly the square of the gradient acting on the noise, i.e., $\nabla_{nm}^2 = \nabla_{nk} \nabla_{km}$ ⁶⁰—this is the Einstein relation. Here ξ is unit white noise, and we use the second-order stencil for ∇_{nm} ,

$$\left(\frac{1}{12}, -\frac{2}{3}, 0, \frac{2}{3}, -\frac{1}{12} \right) \quad (\text{C2})$$

This has the disadvantage that high-frequency oscillations are not detected by ∇^2 as it only measures sites at an even number of lattice sites away from the diagonal. We therefore apply a different operator, $\tilde{\nabla}^2$ with the stencil

$$\left(-\frac{1}{12}, \frac{4}{3}, -\frac{5}{2}, \frac{4}{3}, -\frac{1}{12} \right) \quad (\text{C3})$$

to the surface tension term, which becomes $\nabla^2 \tilde{\nabla}^2 \varphi$. This ensures that high-frequency oscillations have an energetic cost and avoid a decoupling of the even and odd lattice sites.

- ¹S. Ramaswamy, “The Mechanics and Statistics of Active Matter,” *Annu. Rev. Condens. Matter Phys.* **1**, 323–345 (2010).
- ²R. Golestanian, “Phoretic Active Matter,” in *Active Matter and Nonequilibrium Statistical Physics: Lecture Notes of the Les Houches Summer School: Volume 112, September 2018*, edited by J. Tailleur, G. Gompper, M. C. Marchetti, J. M. Yeomans, and C. Salomon (Oxford University Press, 2022) pp. 230–293.
- ³H. Chaté and B. Mahault, “Dry, Aligning, Dilute, Active Matter: A Synthetic and Self-contained Overview,” in *Active Matter and Nonequilibrium Statistical Physics: Lecture Notes of the Les Houches Summer School: Volume 112, September 2018*, edited by J. Tailleur, G. Gompper, M. C. Marchetti, J. M. Yeomans, and C. Salomon (Oxford University Press, 2022) pp. 3–51.
- ⁴G. Gompper, R. G. Winkler, T. Speck, A. Solon, C. Nardini, F. Peruani, H. Löwen, R. Golestanian, U. B. Kaupp, L. Alvarez, T. Kjörboe, E. Lauga, W. C. K. Poon, A. DeSimone, S. Muiños-Landin, A. Fischer, N. A. Söker, F. Cichos, R. Kapral, P. Gaspard, M. Ripoll, F. Sagues, A. Doostmohammadi, J. M. Yeomans, I. S. Aranson, C. Bechinger, H. Stark, C. K. Hemelrijk, F. J. Nedelec, T. Sarkar, T. Aryaksama, M. Lacroix, G. Duclos, V. Yashunsky, P. Silberzan, M. Arroyo, and S. Kale, “The 2020 motile active matter roadmap,” *J. Phys.: Condens. Matter* **32**, 193001 (2020).
- ⁵M. E. Cates and C. Nardini, “Active phase separation: new phenomenology from non-equilibrium physics,” (2024).
- ⁶R. Soto and R. Golestanian, “Self-Assembly of Catalytically Active Colloidal Molecules: Tailoring Activity Through Surface Chemistry,” *Phys. Rev. Lett.* **112**, 068301 (2014).
- ⁷R. Soto and R. Golestanian, “Self-assembly of active colloidal molecules with dynamic function,” *Phys. Rev. E* **91**, 052304 (2015).
- ⁸J. Agudo-Canalejo and R. Golestanian, “Active Phase Separation in Mixtures of Chemically Interacting Particles,” *Phys. Rev. Lett.* **123**, 018101 (2019).
- ⁹S. Saha, S. Ramaswamy, and R. Golestanian, “Pairing, waltzing and scattering of chemotactic active colloids,” *New J. Phys.* **21**, 063006 (2019).
- ¹⁰C. H. Meredith, P. G. Moerman, J. Groenewold, Y.-J. Chiu, W. K. Kegel, A. van Blaaderen, and L. D. Zarzar, “Predator-prey interactions between droplets driven by non-reciprocal oil exchange,” *Nat. Chem.* **12**, 1136–1142 (2020).
- ¹¹N. Uchida and R. Golestanian, “Synchronization and collective dynamics in a carpet of microfluidic rotors,” *Phys. Rev. Lett.* **104**, 178103 (2010).
- ¹²D. J. Hickey, R. Golestanian, and A. Vilfan, “Nonreciprocal interactions give rise to fast cilium synchronization in finite systems,” *Proceedings of the National Academy of Sciences* **120** (2023), 10.1073/pnas.2307279120.
- ¹³M. Fruchart, R. Hanai, P. B. Littlewood, and V. Vitelli, “Non-reciprocal phase transitions,” *Nature* **592**, 363–369 (2021).
- ¹⁴B. Derrida, E. Gardner, and A. Zippelius, “An Exactly Solvable Asymmetric Neural Network Model,” *Europhys. Lett.* **4**, 167–173 (1987).
- ¹⁵H. Sompolinsky and I. Kanter, “Temporal Association in Asymmetric Neural Networks,” *Phys. Rev. Lett.* **57**, 2861–2864 (1986).
- ¹⁶V. Ouazan-Reboul, J. Agudo-Canalejo, and R. Golestanian, “Self-organization of primitive metabolic cycles due to non-reciprocal interactions,” *Nat. Commun.* **14**, 4496 (2023).
- ¹⁷V. Ouazan-Reboul, R. Golestanian, and J. Agudo-Canalejo, “Network effects lead to self-organization in metabolic cycles of self-repelling catalysts,” *Phys. Rev. Lett.* **131**, 128301 (2023).
- ¹⁸V. Ouazan-Reboul, R. Golestanian, and J. Agudo-Canalejo, “Interaction-motif-based classification of self-organizing metabolic cycles,” *New J. Phys.* **25**, 103013 (2023).
- ¹⁹C. Scheibner, A. Souslov, D. Banerjee, P. Surowka, W. T. M. Irvine, and V. Vitelli, “Odd elasticity,” *Nat. Phys.* **16**, 475–480 (2020).
- ²⁰M. Fruchart, C. Scheibner, and V. Vitelli, “Odd Viscosity and Odd Elasticity,” *Annu. Rev. Condens. Matter Phys.* **14**, 471–510 (2023).
- ²¹T. H. Tan, A. Mietke, J. Li, Y. Chen, H. Higinbotham, P. J. Foster, S. Gokhale, J. Dunkel, and N. Fakhri, “Odd dynamics of living chiral crystals,” *Nature* **607**, 287–293 (2022).
- ²²A. Melzer, V. A. Schweigert, I. V. Schweigert, A. Homann, S. Peters, and A. Piel, “Structure and stability of the plasma crystal,” *Phys. Rev. E* **54**, R46–R49 (1996).
- ²³A. Melzer, V. A. Schweigert, and A. Piel, “Transition from Attractive to Repulsive Forces between Dust Molecules in a Plasma Sheath,” *Phys. Rev. Lett.* **83**, 3194–3197 (1999).
- ²⁴E. A. Lisin, O. F. Petrov, E. A. Sametov, O. S. Vaulina, K. B. Statsenko, M. M. Vasiliev, J. Carmona-Reyes, and T. W. Hyde, “Experimental study of the nonreciprocal effective interactions between microparticles in an anisotropic plasma,” *Sci Rep* **10**, 13653 (2020).
- ²⁵N. P. Kryuchkov, L. A. Mistryukova, A. V. Sapelkin, and S. O. Yurchenko, “Strange attractors induced by melting in systems with nonreciprocal effective interactions,” *Phys. Rev. E* **101**, 063205 (2020).
- ²⁶R. Hanai, D. Ootsuki, and R. Tazai, “Photoinduced non-reciprocal magnetism,” (2024), arXiv:2406.05957 [cond-mat].
- ²⁷T. Nadolny, C. Bruder, and M. Brunelli, “Nonreciprocal Synchronization of Active Quantum Spins,” *Phys. Rev. X* **15**, 011010 (2025).
- ²⁸R. Belyansky, C. Weis, R. Hanai, P. B. Littlewood, and A. A. Clerk, “Phase Transitions in Nonreciprocal Driven-Dissipative Condensates,” (2025), arXiv:2502.05267 [quant-ph].
- ²⁹I. S. Aranson and L. Kramer, “The world of the complex Ginzburg-Landau equation,” *Rev. Mod. Phys.* **74**, 99–143 (2002).
- ³⁰S. Osat and R. Golestanian, “Non-reciprocal multifarious self-organization,” *Nature Nanotechnology* **18**, 79–85 (2022).
- ³¹J. T. Young, A. V. Gorshkov, and M. Maghrebi, “Nonequilibrium universality of the nonreciprocally coupled $\mathbf{O}(\mathbf{n}_1) \times \mathbf{O}(\mathbf{n}_2)$ model,” (2024), arXiv:2411.12680 [cond-mat].
- ³²M. K. Johnsrud and R. Golestanian, “Fluctuation Dissipation Relations for the Non-Reciprocal Cahn-Hilliard Model,” (2025), arXiv:2502.02524 [cond-mat].
- ³³M. K. Johnsrud and R. Golestanian, “Fluctuation Dissipation Relations for Active Field Theories,” (2025), arXiv:2409.14977 [cond-mat].
- ³⁴Y. Avni, M. Fruchart, D. Martin, D. Seara, and V. Vitelli, “The non-reciprocal Ising model,” (2023), arXiv:2311.05471 [cond-mat, physics:nlm].
- ³⁵S. Osat, J. Metson, M. Kardar, and R. Golestanian, “Escaping kinetic traps using nonreciprocal interactions,” *Phys. Rev. Lett.* **133**, 028301 (2024).
- ³⁶T. Kato, *Perturbation Theory for Linear Operators*, *Classics in Mathematics* (Springer, Berlin, 1995).
- ³⁷W. D. Heiss, “The physics of exceptional points,” *J. Phys. A: Math. Theor.* **45**, 444016 (2012).
- ³⁸W. D. Heiss and A. L. Sannino, “Transitional regions of finite Fermi systems and quantum chaos,” *Phys. Rev. A* **43**, 4159–4166 (1991).
- ³⁹C. M. Bender and S. Boettcher, “Real Spectra in Non-Hermitian Hamiltonians Having \mathcal{PT} Symmetry,” *Phys. Rev. Lett.* **80**, 5243–5246 (1998).
- ⁴⁰V. V. Konotop, J. Yang, and D. A. Zezyulin, “Nonlinear waves in \mathcal{PT} -symmetric systems,” *Rev. Mod. Phys.* **88**, 035002 (2016).
- ⁴¹S. V. Suchkov, A. A. Sukhorukov, J. Huang, S. V. Dmitriev, C. Lee, and Y. S. Kivshar, “Nonlinear switching and solitons in \mathcal{PT} -symmetric photonic systems,” *Laser Photonics Rev.* **10**, 177–213 (2016).
- ⁴²H. Cartarius, J. Main, and G. Wunner, “Exceptional Points in Atomic Spectra,” *Phys. Rev. Lett.* **99**, 173003 (2007).
- ⁴³S. Saha, J. Agudo-Canalejo, and R. Golestanian, “Scalar Active Mixtures: The Nonreciprocal Cahn-Hilliard Model,” *Phys. Rev. X* **10**, 041009 (2020).
- ⁴⁴Z. You, A. Baskaran, and M. C. Marchetti, “Nonreciprocity as a generic route to traveling states,” *Proc. Natl. Acad. Sci. U.S.A.* **117**, 19767–19772 (2020).

- ⁴⁵R. Hanai and P. B. Littlewood, “Critical fluctuations at a many-body exceptional point,” *Phys. Rev. Research* **2**, 033018 (2020).
- ⁴⁶C. P. Zelle, R. Daviet, A. Rosch, and S. Diehl, “Universal Phenomenology at Critical Exceptional Points of Nonequilibrium $O(n)$ Models,” *Phys. Rev. X* **14**, 021052 (2024).
- ⁴⁷J. T. Young, A. V. Gorshkov, M. Foss-Feig, and M. F. Maghrebi, “Nonequilibrium Fixed Points of Coupled Ising Models,” *Phys. Rev. X* **10**, 011039 (2020).
- ⁴⁸J. W. Cahn and J. E. Hilliard, “Free Energy of a Nonuniform System. I. Interfacial Free Energy,” *J. Chem. Phys.* **28**, 258–267 (1958).
- ⁴⁹J. W. Cahn, “Free Energy of a Nonuniform System. II. Thermodynamic Basis,” *J. Chem. Phys.* **30**, 1121–1124 (1959).
- ⁵⁰T. Frohoff-Hülsmann, J. Wrembel, and U. Thiele, “Suppression of coarsening and emergence of oscillatory behavior in a Cahn-Hilliard model with nonvariational coupling,” *Phys. Rev. E* **103**, 042602 (2021).
- ⁵¹G. Pisegna, S. Saha, and R. Golestanian, “Emergent polar order in nonpolar mixtures with nonreciprocal interactions,” *Proc. Natl. Acad. Sci. U.S.A.* **121**, e2407705121 (2024).
- ⁵²N. Rana and R. Golestanian, “Defect Solutions of the Nonreciprocal Cahn-Hilliard Model: Spirals and Targets,” *Phys. Rev. Lett.* **133**, 078301 (2024).
- ⁵³P. C. Hohenberg and B. I. Halperin, “Theory of dynamic critical phenomena,” *Rev. Mod. Phys.* **49**, 435–479 (1977).
- ⁵⁴S. Saha and R. Golestanian, “Effervescent waves in a binary mixture with non-reciprocal couplings,” (2022), arXiv:2208.14985 [cond-mat].
- ⁵⁵Supplemental Material (link to be inserted).
- ⁵⁶W. Heiss, “Exceptional Points – Their Universal Occurrence and Their Physical Significance,” *Czech. J. Phys.* **54**, 1091–1099 (2004).
- ⁵⁷S. H. Strogatz, *Nonlinear Dynamics and Chaos: With Applications to Physics, Biology, Chemistry, and Engineering* (CRC Press, 2018).
- ⁵⁸A. Bray, “Theory of phase-ordering kinetics,” *Adv. Phys.* **43**, 357–459 (1994).
- ⁵⁹Y. Duan, J. Agudo-Canalejo, R. Golestanian, and B. Ma-hault, “Dynamical Pattern Formation without Self-Attraction in Quorum-Sensing Active Matter: The Interplay between Nonreciprocity and Motility,” *Phys. Rev. Lett.* **131**, 148301 (2023).
- ⁶⁰C. Nardini, É. Fodor, E. Tjhung, F. van Wijland, J. Tailleur, and M. E. Cates, “Entropy Production in Field Theories without Time-Reversal Symmetry: Quantifying the Non-Equilibrium Character of Active Matter,” *Phys. Rev. X* **7**, 021007 (2017).